ChemPhysMater 3 (2024) 118–124

Contents lists available at ScienceDirect

ChemPhysMater

journal homepage: https://www.keaipublishing.com/en/journals/chemphysmater/

Research Article

Hierarchical assembly of NiFe-PB-derived bimetallic phosphides on 3D Ti_3C_2 MXene ribbon networks for efficient oxygen evolution

Chulong Jin[a,#], Hanlei Peng[a,#], Xiaojun Zeng[a,*], Zhenyuan Liu[b], Deng Ding[c,*]

[a] School of Materials Science and Engineering, Jingdezhen Ceramic University, Jingdezhen 333403, China
[b] School of Materials Science and Engineering, Jiangsu University of Science and Technology, Zhenjiang 212100, China
[c] College of Chemistry and Environmental Engineering, Wuhan Polytechnic University, Wuhan 430023, China

ARTICLE INFO

Keywords:
Metal phosphides
Prussian blue nanocubes
Ti_3C_2 MXene ribbons
Interfacial matching
OER

ABSTRACT

The development of MXene-based heterostructures for electrocatalysis has garnered significant attention owing to their potential as high-performance catalysts that play a pivotal role in hydrogen energy. Herein, we present a multistep strategy for the synthesis of a Ti_3C_2 MXene ribbon/$NiFeP_x$ @graphitic N-doped carbon (NC) heterostructure that enables the formation of three-dimensional (3D) Ti_3C_2 MXene ribbon networks and bimetallic phosphide nanoarrays. With the assistance of HF etching and KOH shearing, the MXene sheets were successfully transformed into 3D MXene networks with interlaced MXene ribbons. Notably, a hydrothermal method, ion exchange route, and phosphorization process were used to anchor $NiFeP_x$@NC nanocubes derived from $Ni(OH)_2$/NiFe-based Prussian blue (NiFe-PB) onto the MXene ribbon network. The resulting MXene ribbon/$NiFeP_x$@NC heterostructure demonstrated enhanced oxygen evolution reaction (OER) activity, characterized by a low overpotential (164 mV at a current density of 10 mA cm^{-2}) and a low Tafel slope (45 mV dec^{-1}). At the same time, the MXene ribbons/$NiFeP_x$@NC heterostructure exhibited outstanding long-term stability, with a 12 mV potential decay after 5000 cyclic voltammetry (CV) cycles. This study provides a robust pathway for the design of efficient MXene-based heterostructured electrocatalysts for water splitting.

1. Introduction

Hydrogen is a promising, environment-friendly, and sustainable energy source. Among the numerous hydrogen production methods, electrochemical water splitting is widely recognized as an ideal approach for hydrogen generation [1–3]. However, the entire process of electrochemical water splitting is constrained by the poor kinetics of the anodic oxygen evolution reaction (OER), which is a four-electron process and poses a significant hurdle to achieving efficient hydrogen production [4–6]. Noble metal-based catalysts, such as RuO_2 and IrO_2, are presently robust OER catalysts, but their widespread adoption is impeded by their considerable cost, limited availability, and inadequate durability [7–9]. Therefore, significant research effort has been dedicated to the development of cost-effective and highly efficient catalysts.

Prussian blue analogs (PBAs), which are typical examples of metal-organic frameworks (MOFs), have multiple transition metal active centers. These atoms are strongly interconnected within the framework, enabling them to achieve more accessible active sites and generate unexpected synergistic effects [10–12]. Furthermore, PBAs can be further modified and converted into other polymetallic compounds through chemical processes [13–15]. In particular, PBA-derived transition metal phosphides are prominent on account of their high specific surface area, rich pore structure, highly dispersed active sites, and considerable conductivity [16–19]. However, PBAs synthesized via chemical precipitation typically exist in powder form and require coating onto a conductive substrate using a polymeric binder for electrocatalytic processes. This leads to agglomeration, thereby reducing the active surface area and resulting in suboptimal catalytic performance [20,21]. In addition, MOF-derived multivariate transition metal phosphides have shown considerable electrocatalytic activity due to their unique electronic structures and abundant active sites [22]. To this end, it is necessary to explore a reliable substrate to disperse PBAs and achieve good interfacial binding behavior to decrease their aggregation, thereby accelerating their electrocatalytic kinetics.

MXenes ($Ti_3C_2T_x$), which are novel two-dimensional (2D) transition-metal-based carbides or nitrides, exhibit excellent electrical conductivity, considerable surface area, and remarkable chemical stability. Additionally, the surface of MXenes obtained through certain etching processes contains a large number of functional groups (denoted as T_x), such as hydroxyl (–OH), fluorine (–F), and oxygen (–O), which enable

* Corresponding authors.
E-mail addresses: zengxiaojun@jcu.edu.cn (X. Zeng), dingdeng211@foxmail.com (D. Ding).
# These authors contributed equally to this work.

https://doi.org/10.1016/j.chphma.2023.09.001
Received 7 August 2023; Received in revised form 17 September 2023; Accepted 21 September 2023
Available online 26 September 2023

MXenes to form composites with other materials and achieve excellent synergistic effects [23–26]. However, due to the robust van der Waals forces between the layered $Ti_3C_2T_x$ MXene sheets, they tend to aggregate, leading to a substantial reduction in the available active site loading area. Thus, developing a reliable process for obtaining a novel MXene structure is an effective route to overcome the aforementioned bottlenecks and achieve better catalytic performance [27–29]. For example, Zeng and co-worker reported a honeycomb-like MXene/$NiFeP_x$-NC heterostructure, which combined highly dispersed $NiFeP_x$ nanoparticles and layered MXene and exhibited a remarkable OER activity with an overpotential of 240 mV at a current density of 10 mA cm^{-2} [30]. Li et al. loaded a large number of NiFeCoP nanoparticles onto MXene to promote the OER [31]. Yue et al. grew mesoporous NiCoP nanosheets on MXene using an in-situ interface growth strategy and subsequent phosphorization; the obtained MXene@mNiCoP exhibited excellent OER activity [32].

In this study, we propose an integrated electrode composed of MXene ribbons, $NiFeP_x$@graphitic N-doped carbon (NC) derived from Ti_3C_2 MXene sheets, and $Ni(OH)_2$/NiFe-based Prussian blue (NiFe-PB) as a highly efficient OER electrocatalyst for promoting pollution-free hydrogen production. Owing to the presence of unsaturated coordination sites on the surface of the $Ni(OH)_2$ sheets, NiFe-PB was grown in situ on the $Ni(OH)_2$ surface. The as-obtained $NiFeP_x$@NC was tightly anchored to the MXene ribbon network, promoting electron transfer and structural stability. Simultaneously, the obtained open-pore structured bimetallic phosphide nanoarrays can increase mass transfer and expose more active sites. Thus, the target MXene ribbon/$NiFeP_x$@NC heterostructure exhibited remarkable performance in terms of OER activity and stability. MXene ribbons/$NiFeP_x$@NC can achieve an overpotential of 164 mV at a current density of 10 mA cm^{-2}, which is superior to many reported non-precious metal OER catalysts. The proposed method not only avoids the aggregation of PBA-derived transition metal phosphides, but also strengthens the bonding and contact of heterogeneous interfaces, thereby exposing active sites and improving the long-term stability of the catalyst.

2. Experimental section

2.1. Chemicals

Ti_3AlC_2 MAX (≥ 99%, 200 mesh) was purchased from Laizhou Kai Xi Ceramic Materials Co., Ltd. Nickel nitrate hexahydrate ($Ni(NO_3)_2{\cdot}6H_2O$, ≥ 98%), potassium ferricyanide ($K_3[Fe(CN)_6]$, ≥ 99.5%), hexamethylenetetramine (HMT, ≥ 99%), trisodium citrate dihydrate ($Na_3C_6H_5O_7{\cdot}2H_2O$, NaAc, ≥ 99%), sodium hypophosphite monohydrate ($NaH_2PO_2{\cdot}H_2O$, ≥ 99%), potassium hydroxide (KOH, 95%), and hydrofluoric acid (HF, 40%) were purchased from Sinopharm Chemical Reagent Co., Ltd. All reagents were used directly without further purification.

2.2. Synthesis of MXene sheets

0.5 g of Ti_3AlC_2 MAX was slowly introduced into a 100 mL Teflon liner containing 60 mL of concentrated HF and stirred at room temperature for 72 h. The resulting mixture was centrifuged to isolate the product, which was washed multiple times with deionized water. Finally, the products were subjected to vacuum drying at 60 ˚C for 12 h to obtain the Ti_3C_2 MXene sheets.

2.3. Synthesis of MXene ribbons

0.5 g of Ti_3C_2 MXene sheets were dispersed in 60 mL of a KOH solution (6 M) and stirred for 72 h. The resulting mixture was centrifuged to isolate the product, which was washed multiple times with deionized water and dried in a vacuum oven at 60 ˚C for 24 h to obtain the Ti_3C_2 MXene ribbons.

2.4. Synthesis of the MXene ribbons/$Ni(OH)_2$ heterostructure

0.04 g of Ti_3C_2 MXene ribbons were added to 60 mL of ethanol, followed by stirring for 30 min and sonication for 30 min. 0.1454 g of $Ni(NO_3)_2{\cdot}6H_2O$ and 0.56 g of HMT were subsequently added to the aforementioned solution and stirred for 15 min. The solution was transferred to a Teflon-lined autoclave with a volume of 100 mL and left to react at 120 ˚C for 4 h; the resulting product was centrifuged, washed multiple times with ethanol and dried in a vacuum oven at 60 ˚C overnight to obtain the Ti_3C_2 MXene ribbons/$Ni(OH)_2$ heterostructures.

2.5. Synthesis of the MXene ribbons/$Ni(OH)_2$/NiFe-PB heterostructure

0.6615 g of NaAc and 0.436 g of $Ni(NO_3)_2{\cdot}6H_2O$ were mixed in 50 mL of deionized water to create a homogeneous solution. 50 mL of deionized water containing 0.329 g of $K_3[Fe(CN)_6]$ was slowly added to the aforementioned solution and stirred for 15 min to obtain a clear fluorescent green solution. 0.02 g of MXene ribbons/$Ni(OH)_2$ was dispersed into the solution, which was then sealed in a beaker, kept at 40 ˚C for 1 h and incubated for 10 h at room temperature. The resulting powder was washed multiple times with deionized water and ethanol and then dried in a vacuum oven at 60 ˚C for 12 h to obtain the Ti_3C_2 MXene ribbon/Ni $(OH)_2$/NiFe-based Prussian blue (NiFe-PB) heterostructures.

2.6. Synthesis of the MXene ribbons/$NiFeP_x$@NC heterostructure

The synthesized MXene ribbon/$Ni(OH)_2$/NiFe-PB heterostructures and sodium hypophosphite (0.5 g) were placed in two porcelain vessels and transferred to a tube furnace. In this system, the sodium hypophosphite was used as a phosphorus source and participated in the reaction via gas-phase volatilization. The products were heated to 350 ˚C at a heating rate of 2 ˚C min^{-1} and kept for 2 h under a N_2 atmosphere. Finally, the Ti_3C_2 MXene ribbon/$NiFeP_x$@NC heterostructures were obtained. Similarly, MXene ribbons/$NiFeP_x$@NC structures with different MXene ribbon contents (20 and 60 mg) were prepared to optimize the electrocatalytic properties of the catalysts. Pure NiFe-PB and $NiFeP_x$@NC catalysts were synthesized for comparison. $NiFeP_x$@NC was obtained by pyrolysis of NiFe-PB at 350 ˚C by placing sodium hypophosphite on the upstream side of the tube furnace.

2.7. Materials characterization

The crystal structures of the samples were examined using X-ray diffraction (XRD; D8 Advance, Bruker, Germany). The microstructures and morphologies of the samples were observed by field-emission scanning electron microscopy (FE-SEM; HITACHI, SU8010, Japan) and transmission electron microscopy (TEM; JEM-2100F, Japan). Chemical elemental mapping analysis of the samples was performed using X-ray photoelectron spectroscopy (XPS; Thermo Escalab 250Xi) and energy-dispersive X-ray spectroscopy (EDS; Oxford Instruments, Xplore, UK) coupled to the SEM equipment.

2.8. Electrochemical measurements

The electrochemical properties of the catalysts and the commercial RuO_2 were assessed using a three-electrode cell controlled by a CHI760E electrochemical workstation connected to a rotating device (RRDE-3A; ALS Inc., Tokyo, Japan). The electrolyte was a KOH solution (1 M) saturated with oxygen. The counter and reference electrodes were composed of platinum wire and Ag/AgCl, respectively. The working electrode was prepared by combining 4 mg of the catalyst with 1 mL of a Nafion solution (5 wt.%) and sonicating the mixture for 2 h to obtain the catalyst ink. Subsequently, the catalyst ink was dropped onto a glassy carbon electrode with a diameter of 3 mm, resulting in a catalyst loading of 0.2 mg cm^{-2}. Linear scanning voltammetry (LSV) curves were recorded at a scan rate of 2 mV s^{-1}. The

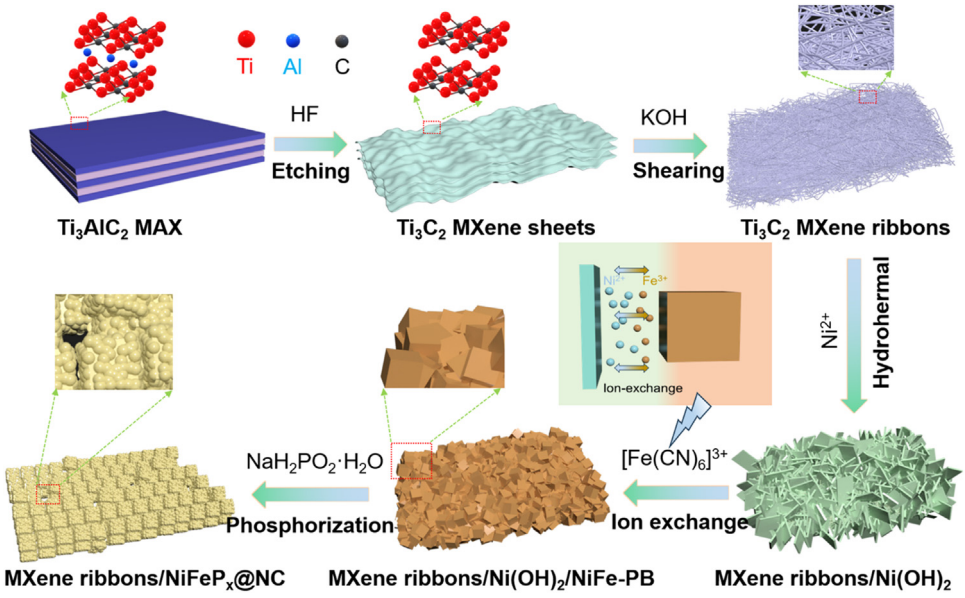

Fig. 1. Scheme showing the fabrication process of the MXene ribbons/$NiFeP_x$@NC heterostructure.

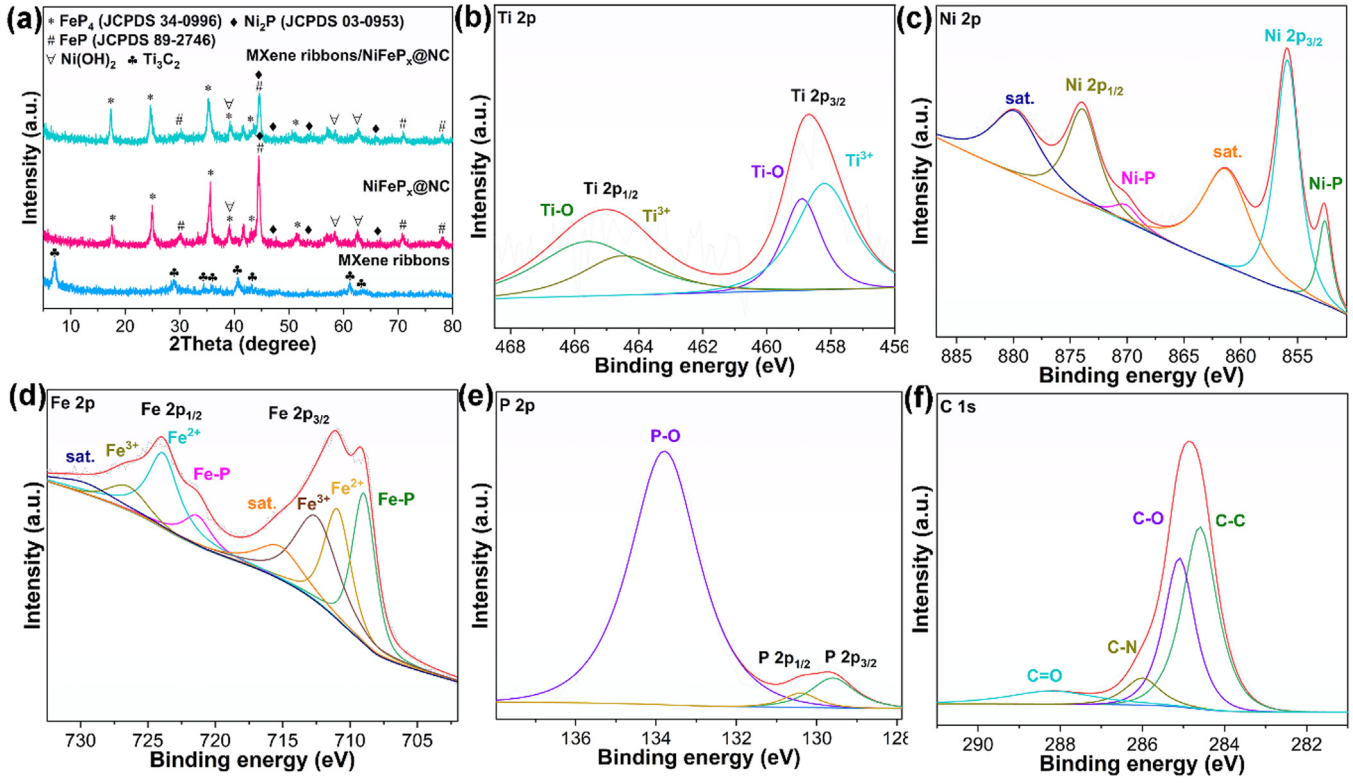

Fig. 2. (a) XRD patterns of the catalysts. High-resolution XPS spectra of (b) Ti 2p, (c) Ni 2p, (d) Fe 2p, (e) P 2p, and (f) C 1s for the MXene ribbons/$NiFeP_x$@NC heterostructure.

double-layer capacitance (C_{dl}) was analyzed by cyclic voltammetry (CV) curves at scan rates ranging from 20 to 200 mV s^{-1}. The electrochemical surface area (ECSA) value was calculated based on the following equation: ECSA = C_{dl}/C_s (C_s represents the specific capacitance, C_s = 0.04 mF cm^{-2} in a 1 M KOH solution) [33]. The electrochemical impedance spectra (EIS) were acquired with an open circuit potential and an AC voltage of 5 mV across a frequency range of 0.01 Hz to 100 kHz. The stability of the samples was assessed by chronoamperometry at a constant potential of 1.394 V (vs. reversible hydrogen electrode (RHE)). The reference electrode was converted to the RHE using the following equation: $E_{RHE} = E_{Ag/AgCl} + 0.0591 \times pH + 0.197$.

3. Results and discussion

Ti_3C_2 MXene ribbon/$NiFeP_x$@NC heterostructures were prepared using a hydrothermal method, ion exchange route, and phosphorization process, as shown in Fig. 1. Typically, Ti_3AlC_2 MAX species were etched with HF to obtain Ti_3C_2 MXene sheets, as previously described [34].

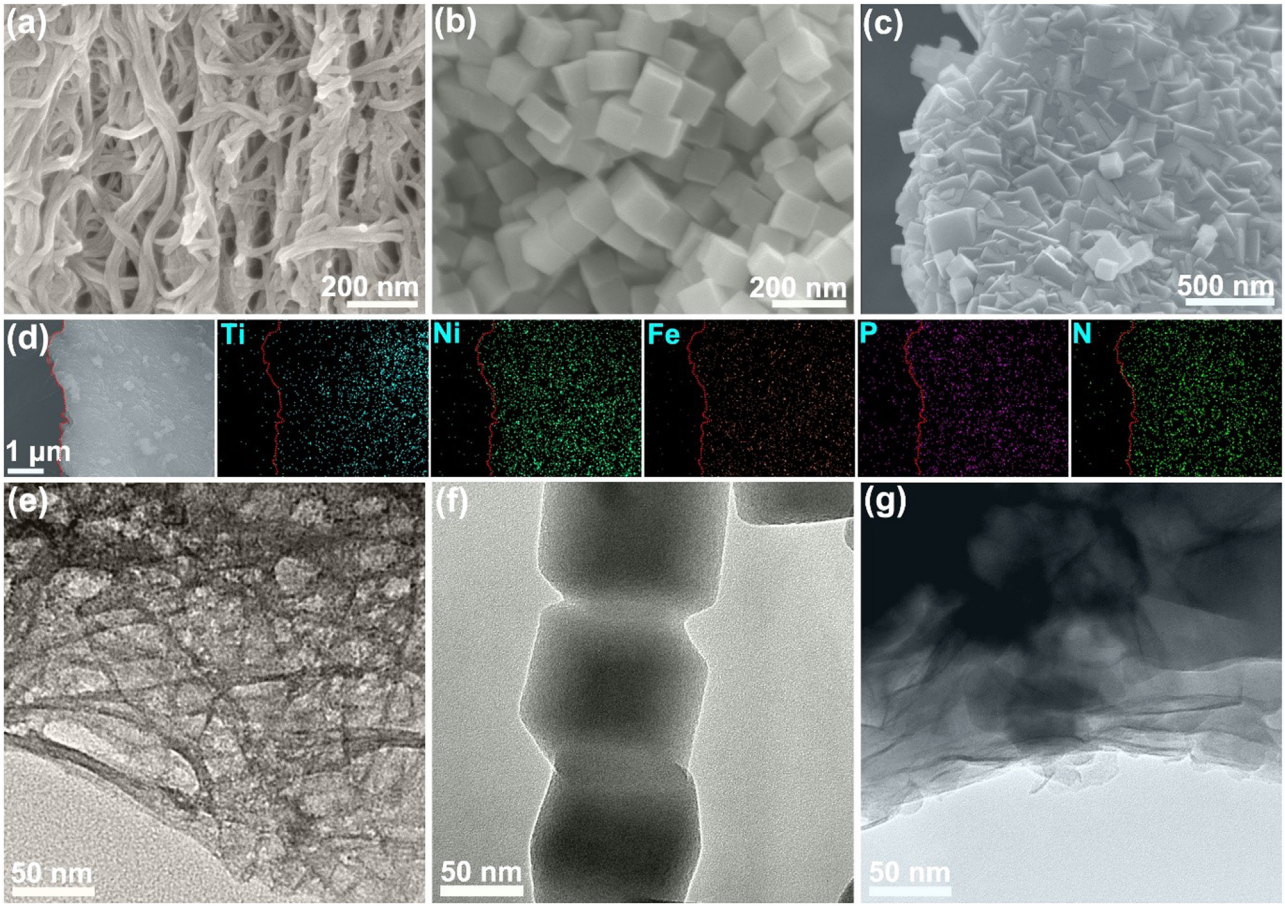

Fig. 3. (a)–(c) SEM images and (e)–(g) TEM images of (a)(e) MXene ribbons, (b)(f) NiFe-PB, and (c)(g) MXene ribbons/$NiFeP_x$@NC heterostructure. (d) EDS elemental mapping image of the MXene ribbons/$NiFeP_x$@NC heterostructure.

Subsequently, the Ti_3C_2 sheets were transformed into three-dimensional (3D) MXene networks with interlaced Ti_3C_2 ribbons by the "shearing effect" of the KOH solution [35,36]. $Ni(OH)_2$ sheets were grown on MXene ribbons using a hydrothermal method, and NiFe-based Prussian blue (NiFe-PB) nanocubes were grown in situ by ion exchange with the assistance of unsaturated Ni^{2+} ions in the $Ni(OH)_2$ sheets. Finally, the MXene ribbon/$Ni(OH)_2$/NiFe-PB was transformed into MXene ribbon/$NiFeP_x$@NC heterostructures by a low-temperature phosphorization process. Interestingly, the unsaturated coordination sites on the surface of the $Ni(OH)_2$ sheets not only promoted the in situ growth of PB nanocubes but also enhanced the binding of PB nanocubes and MXene ribbon substrates, which facilitated charge transfer and structural stability. During the phosphorization process, bimetallic phosphates ($NiFeP_x$) are formed and coated with graphitic N-doped carbon (NC), which provides good electrical conductivity. These bimetallic phosphide nanoarrays with open-pore structures can expose a large number of active sites and enhance mass transfer, indicating that the target products may be efficient OER electrocatalysts.

The phases of the catalysts were analyzed using the X-ray diffraction (XRD) technique, as illustrated in Figs. 2(a) and S1. The diffraction peaks of the synthesized Ti_3C_2 MXene ribbons were assigned to the Ti_3C_2 MXene phase, in agreement with previous reports [36]. The noticeable diffraction peak at 7.14° indicates the interlayer spacing of the MXene ribbons significantly increased, which further confirmed the successful removal of Al from the MAX species and expansion of the MXene sheets. In the XRD patterns of the MXene ribbon/$NiFeP_x$@NC samples, the detected diffraction peaks can be assigned to Ti_3C_2 MXene, FeP_4 (JCPDS 34-0996), FeP (JCPDS 89-2746), and Ni_2P (JCPDS 03-0953) phases [37–40]. The formation of metal phosphides indicates that the $Ni(OH)_2$/NiFe-PB species were successfully phosphorylated. Furthermore, the pure NiFe-PB-derived $NiFeP_x$@NC samples exhibited diffraction peaks corresponding to the FeP_4, FeP, and Ni_2P phases.

The binding environments of the elements in the samples were examined using X-ray photoelectron spectroscopy (XPS). XPS analysis revealed the presence of Ti, Ni, Fe, P, C, N, and O in the MXene ribbon/$NiFeP_x$@NC heterostructure (Fig. S2), which is consistent with the XRD results mentioned above. Furthermore, the Ni:Fe atomic ratio was approximately 1:1. The high-resolution XPS spectrum of Ti 2p in Fig. 2(b) exhibits two primary peaks, Ti $2p_{3/2}$ (458.7 eV) and Ti $2p_{1/2}$ (464.5 eV), which are attributed to the Ti^{3+} (458.2, 464.4 eV) and Ti–O (458.9, 465.6 eV) bonds, respectively. The appearance of Ti–O bonds was a result of the weak oxidation of the MXene surface [36]. Fig. 2(c) displays the high-resolution XPS spectrum of Ni 2p, revealing the presence of the Ni–P peak (852.7, 870.2 eV), Ni^{2+} peak (855.9, 873.9 eV), and satellite peaks (861.5, 880.0 eV) [36,41]. Similarly, the high-resolution XPS spectrum of Fe 2p can be fitted to Fe–P bonds (708.9, 721.5 eV), Fe^{2+} (711.0, 724.0 eV), Fe^{3+} (712.8, 726.9 eV), and satellite peaks (715.6, 730.2 eV) (Fig. 2(d)) [33,42,43]. As shown in Fig. 2(e), the high-resolution XPS spectrum of P 2p exhibits three distinct peaks; these peaks are identified as P–O bonds at 133.8 eV, and metal-P bonds at 129.5 and 130.5 eV, corresponding to the P $2p_{3/2}$ and P $2p_{1/2}$, respectively [37,44]. The high-resolution C 1s XPS spectrum (Fig. 2(f)) shows four distinct peaks at 284.6, 285.6, 286.0, and 288.2 eV; these peaks correspond to the presence of the C–C, C–O, C–N, and C=O bonds, respectively. In addition, the high-resolution N 1s XPS spectrum identified the presence of pyridine-N (398.0 eV), pyrrole-N (400.0 eV), and graphite-N (401.7 eV), indicating the doping of N heteroatoms in the carbon matrix (Fig. S3).

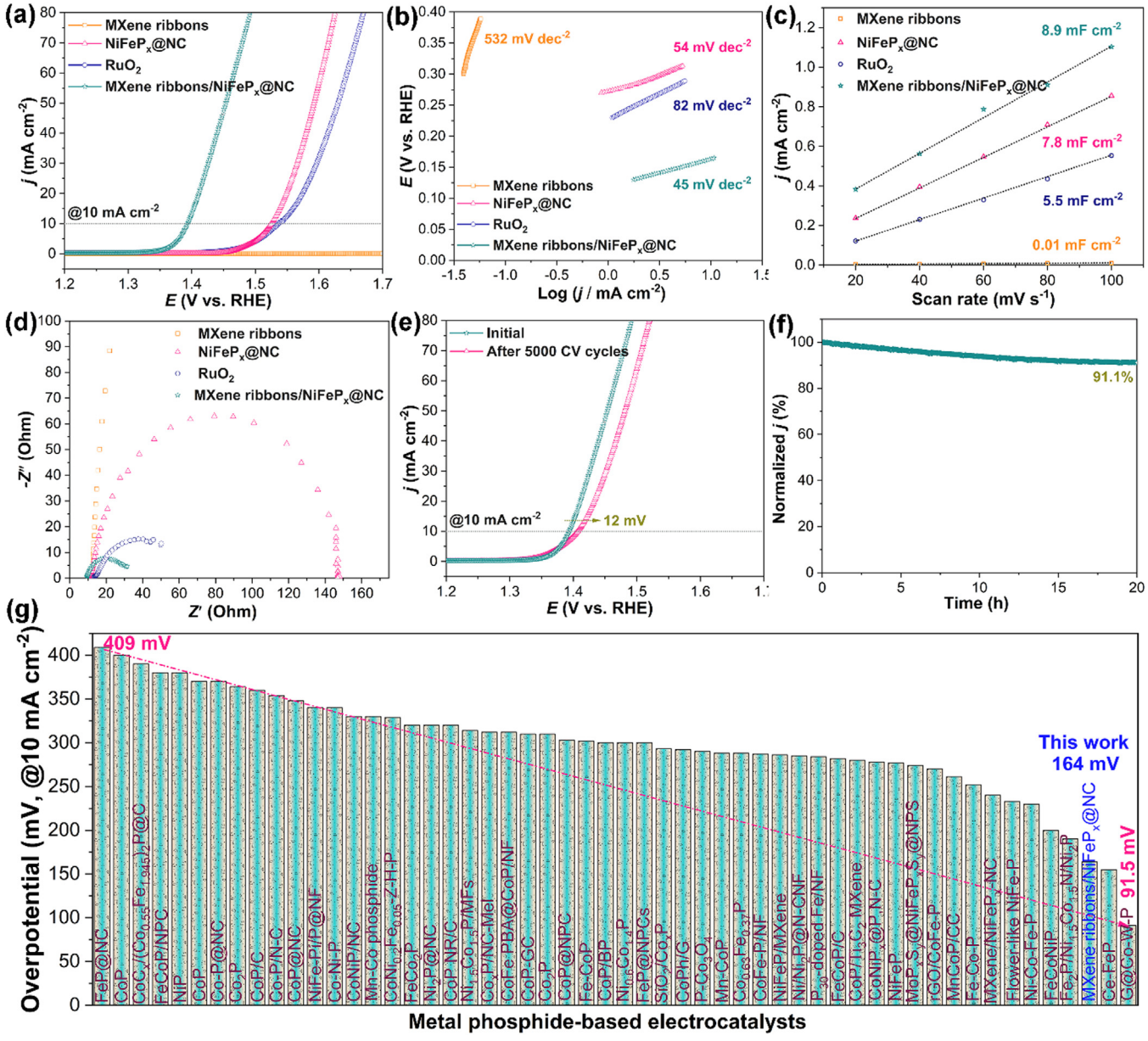

Fig. 4. (a) LSV curves, (b) Tafel slopes, (c) C_{dl} values, and (d) Nyquist plots of MXene ribbons, NiFeP$_x$@NC, commercial RuO$_2$, and MXene ribbons/NiFeP$_x$@NC catalysts. (e) LSV curves of MXene ribbons/NiFeP$_x$@NC before and after 5000 CV cycles. (f) Long-term stability test of the MXene ribbons/NiFeP$_x$@NC heterostructure at a constant potential for 20 h. (g) Overpotential comparison of the MXene ribbons/NiFeP$_x$@NC heterostructure with various advanced metal phosphide-based OER electrocatalysts (@10 mA cm^{-2} in an alkaline electrolyte, see Table S1 for details).

The microstructures and morphologies of the as-prepared catalysts were observed using field-emission scanning electron microscopy (FE-SEM) and transmission electron microscopy (TEM). As depicted in Figs. 3(a) and S4, a large number of MXene ribbons were approximately 17 nm wide and approximately 3 μm long. The numerous ribbons connected with each other were entangled in a 3D network structure and contributed to the electron transfer capability of the catalyst. The TEM images of the MXene ribbons (Figs. 3(e) and S5) revealed the 3D network of the MXene ribbons is cross-linked with numerous pore-like structures, which facilitates contact between the ribbons and electrolytes and allows more loading sites to support the secondary components. In contrast, the SEM images of pure NiFe-PB (Figs. 3(b) and S6) show uniform nanocubes with smooth surfaces and a size of approximately 80 nm, which is corroborated by the NiFe-PB TEM images (Figs. 3(f) and S7). These results indicate that Ni^{2+} ions were successfully coordinated with $[Fe(CN)_6]^{3-}$ ions to form Prussian blue analogs. The SEM images in Fig. S8 show the dense growth of numerous nanoparticles on the surface of the MXene ribbons, confirming a larger number of coordinated sites in the Ni(OH)$_2$ species. As shown in Fig. 3(c), the MXene ribbon/NiFeP$_x$@NC heterostructure exhibited a larger sheet-like structure with abundant irregular cubic PB on the surface. Simultaneously, the PB obtained after phosphorization partially retained its original cubic morphology, while its surface roughened; this suggests that phosphorization does not destroy the 3D network structure. Figs. 3(g) and S9 show that some nanosheets are present in the MXene ribbon/NiFeP$_x$@NC heterostructure, which can be assigned to the products derived from the phosphorization of the Ni(OH)$_2$ sheets. The appearance of nanosheets, such as bridges, is favorable for the bind-

ing of metal phosphides to MXene matrices. The EDS elemental mapping results demonstrated the uniform distribution of Ti, Ni, Fe, P, and N throughout the MXene ribbon/$NiFeP_x$@NC heterostructure (Fig. 3(d)), further indicating that $NiFeP_x$@NC was tightly anchored to the MXene ribbon network.

From the abovementioned composition and morphology characterization of the catalysts, we expected that the MXene ribbon/$NiFeP_x$@NC heterostructure would enable considerable OER performance. Therefore, the electrochemical properties of the target heterostructure and corresponding control samples (MXene ribbons, $NiFeP_x$@NC, and commercial RuO_2 catalysts) were investigated. Fig. 4(a) shows the linear scanning voltammetry (LSV) curves of the catalysts, which show the MXene ribbons do not exhibit OER activity. In contrast, the MXene ribbon/$NiFeP_x$@NC heterostructure exhibited excellent OER activity with an overpotential of 164 mV at a current density of 10 mA cm^{-2}, which is superior to the OER activity of the $NiFeP_x$@NC (295 mV @ 10 mA cm^{-2}) and commercial RuO_2 catalysts (307 mV @ 10 mA cm^{-2}). Apparently, there is a synergistic effect between the MXene ribbons and $NiFeP_x$@NC on the OER performance. The remarkable OER activity of the MXene ribbon/$NiFeP_x$@NC heterostructure indicates it is a better OER electrocatalyst than the majority of previously reported metal-phosphide-based OER catalysts, as illustrated in Fig. 4(g). This is attributed to the synergistic effect of the high conductivity of the 3D MXene ribbons, large surface area of the nanosheet bridge, multiple $NiFeP_x$ species with accessible active sites, and presence of N-doped carbon. Additionally, the optimized experiment showed that the content of MXene ribbons in the heterostructure was adequate (Fig. S10). Notably, the MXene ribbon/$Ni(OH)_2$/NiFe-PB heterostructure pyrolyzed without sodium hypophosphite monohydrate showed poor OER activity, further confirming the positive effect of metal phosphide formation through the phosphorization process.

To delve deeper into the kinetics and mechanisms of the outstanding OER performance of the MXene ribbon/$NiFeP_x$@NC heterostructures we studied the Tafel slopes, C_{dl} values, ECSA values, and electrochemical impedance spectra (EIS) of the catalysts [45,46]. As shown in Fig. 4(b), the MXene ribbons/$NiFeP_x$@NC heterostructure exhibited the lowest Tafel slope (45 mV dec^{-1}), which was lower than those of the MXene ribbons (532 mV dec^{-1}), $NiFeP_x$@NC (54 mV dec^{-1}), and commercial RuO_2 (84 mV dec^{-1}), indicating the more robust kinetics of the MXene ribbon/$NiFeP_x$@NC heterostructures. Moreover, the C_{dl} value of the MXene ribbons/$NiFeP_x$@NC heterostructure is 8.9 mF cm^{-2} (Fig. 4(c)), which is higher than those of other control samples and commercial RuO_2 (5.5 mF cm^{-2}). Thus, the MXene ribbon/$NiFeP_x$@NC heterostructure exhibited the highest ECSA, as shown in Fig. S11. The highest C_{dl} and ECSA values of the MXene ribbon/$NiFeP_x$ @NC heterostructure indicate that it is advantageous in terms of catalytic surface area and active sites [47]. Electrochemical impedance spectroscopy (EIS) in Fig. 4(d) shows that MXene ribbons/$NiFeP_x$@NC enables a small charge-transfer resistance (R_{ct}, 10.7 Ω), revealing its favorable reaction kinetics. The large specific surface area and excellent conductivity promoted the exposure of active sites and accelerated mass transfer. The R_{ct} of $NiFeP_x$@NC and commercial RuO_2 is 123.1 and 37.1 Ω, respectively, which illustrates the coupling of MXene ribbons and metal phosphites. MXene ribbons/$NiFeP_x$@NC exhibited a contact resistance (R_s) of 8.8 Ω, indicating its low resistance and strong ion response [48,49].

Electrocatalytic stability is a crucial parameter when considering the practical applications of OER catalysts. After 5000 cyclic voltammetry (CV) cycles, the MXene ribbons/$NiFeP_x$@NC heterostructure showed a potential decay of only 12 mV at a current density of 10 mA cm^{-2} (Fig. 4(e)), indicating its excellent stability. In addition, the long-term stability of the MXene ribbon/$NiFeP_x$@NC heterostructure was evaluated using chronoamperometry. After continuous OER at a constant potential of 1.394 V (vs. RHE, applied potential at current density of 10 mA cm^{-2}) for 20 h, the current density remained at 91.1%, as shown in Fig. 4(f). The remarkable long-term stability of the MXene ribbon/$NiFeP_x$@NC heterostructure can be ascribed to the stable 3D heterostructure formed by the close combination of the MXene ribbon network and the bimetallic phosphides formed by the ion exchange and phosphorization of the $Ni(OH)_2$/NiFe-PB species. Thus, the MXene ribbon/$NiFeP_x$@NC heterostructure is a promising OER electrocatalyst.

4. Conclusions

In summary, we report a Ti_3C_2 MXene ribbon/$NiFeP_x$@NC heterostructure prepared by a multistep strategy including HF etching, KOH treatment, hydrothermal method, ion-exchange route, and phosphorization. Upon the "shearing effect" induced by the KOH solution, the MXene sheets were successfully transformed into 3D MXene networks with interlaced Ti_3C_2 ribbons. With the growth of $Ni(OH)_2$ nanosheets, NiFe-PB ion exchange, and $Ni(OH)_2$/NiFe-PB phosphorization, the MXene ribbons/$NiFeP_x$@NC heterostructure inherited the open pore structure of the bimetallic phosphide nanoarrays and the strong coupling of heterogeneous interfaces, thereby exposing active sites. Notably, the MXene ribbons/$NiFeP_x$@NC heterostructures in alkaline electrolytes exhibited excellent OER activity with an overpotential of 164 mV at a current density of 10 mA cm^{-2}. The MXene ribbons/$NiFeP_x$@NC heterostructures also exhibited remarkable long-term stability, with a current density retention of 91.1% after 20 h of chronoamperometric measurements. This study provides a robust strategy for designing efficient heterostructures based on MXene electrocatalysts for pollution-free hydrogen production.

Declaration of Competing Interest

The authors declare that they have no known competing financial interests or personal relationships that could have appeared to influence the work reported in this paper.

Acknowledgements

This work was supported by the National Natural Science Foundation of China (No. 22269010), the Jiangxi Provincial Natural Science Foundation (No. 20224BAB214021), the Training Program for Academic and Technical Leaders of Major Disciplines in Jiangxi Province (No. 20212BCJ23020), and the Science and Technology Project of the Jiangxi Provincial Department of Education (No. GJJ211305).

Supplementary materials

Supplementary material associated with this article can be found, in the online version, at doi:10.1016/j.chphma.2023.09.001.

References

[1] Y. Wang, X.P. Li, Zhong Huang, H.Z. Wang, Z.L. Chen, J.F. Zhang, X.R. Zheng, Y.D. Deng, W.B. Hu, Amorphous Mo-doped $NiS_{0.5}Se_{0.5}$ nanosheets@crystalline $NiS_{0.5}Se_{0.5}$ nanorods for high current-density electrocatalytic water splitting in neutral media, Angew. Chem. Int. Ed. 62 (2023) e202215256.
[2] J.Q. Ran, L.C. Wang, M.S. Si, X.L. Liang, D.Q. Gao, Tailoring spin state of perovskite oxides by fluorine atom doping for efficient oxygen electrocatalysis, Small 19 (2023) 2206367.
[3] T.V. Nguyen, M. Tekalgne, T.P. Nguyen, Q.V. Le, S.H. Ahn, S.Y. Kim, Electrocatalysts based on MoS_2 and WS_2 for hydrogen evolution reaction: An overview, Battery Energy 2 (2023) 20220057.
[4] M. Yang, C.H. Zhang, N.W. Li, D.Y. Luan, L. Yu, X.W. Lou, Design and synthesis of hollow nanostructures for electrochemical water splitting, Adv. Sci. 9 (2022) 2105135.
[5] Z.G. Qin, W.X. Liu, W.B. Que, J.X. Feng, W.H. Shi, F.F. Wu, X.H. Cao, Non-noble-metal electrocatalysts for oxygen evolution reaction toward seawater splitting: A review, ChemPhysMater 2 (2023) 185–196.
[6] X.J. Zeng, J.L. Shui, X.F. Liu, Q.T. Liu, Y.C. Li, J.X. Shang, L.R. Zheng, R.H. Yu, Single-atom to single-atom grafting of Pt_1 onto Fe-N_4 center: Pt_1@Fe-N-C multifunctional electrocatalyst with significantly enhanced properties, Adv. Energy Mater. 8 (2018) 1701345.
[7] H. Yang, X.T. Han, A.I. Douka, L. Huang, L.Q. Gong, C.f. Xia, H.S. Park, B.Y. Xia, Advanced oxygen electrocatalysis in energy conversion and storage, Adv. Funct. Mater. 31 (2021) 2007602.
[8] Y.Y. Xie, C. Yu, X.B. Zhang, G.B. Gu, J.H. Yu, Y. Yang, J.S. Qiu, Processable hydroxide ink with oriented microstructure, Adv. Mater. (2023) 10.1002/adma.202305871.

[9] M.Y. Chen, X.P. Wang, X.C. Lou, C.Y. Zhang, M.H. Cao, L. Wang, Y.Y. Li, S.B. Liu, T.K. Sham, Q. Zhang, J.X. Chen, Site-selective polyolefin hydrogenolysis on atomic Ru for methanation suppression and liquid fuel production, Research 6 (2023) 0032.

[10] D.N. Zhao, Y.Z. Lu, D.G. Ma, Effects of structure and constituent of prussian blue analogs on their application in oxygen evolution reaction, Molecules 25 (2020) 2304.

[11] Y.Q. Wang, J.Z. Ma, J. Wang, S. Chen, H.S. Wang, J.T. Zhang, Interfacial scaffolding preparation of hierarchical PBA-based derivative electrocatalysts for efficient water splitting, Adv. Energy Mater. 9 (2019) 1802939.

[12] Y.R. Ji, Y.F. Guo, X. Liu, P.F. Wang, T.F. Yi, Insights on rational design and regulation strategies of Prussian blue analogues and their derivatives towards high-performance electrocatalysts, Chem. Eng. J. 471 (2023) 144743.

[13] B. Bornamehr, V. Presser, A.J.G. Zarbin, Y. Yamauchi, S. Husmann, Prussian blue and its analogues as functional template materials: Control of derived structure compositions and morphologies, J. Mater. Chem. A 11 (2023) 10473–10492.

[14] L. Han, X.Y. Yu, X.W. Lou, Formation of Prussian-blue-analog nanocages via a direct etching method and their conversion into Ni-Co-mixed oxide for enhanced oxygen evolution, Adv. Mater. 28 (2016) 4601–4605.

[15] S.Q. Wang, W.Y. Huo, H.C. Feng, X.F. Zhou, F. Fang, Z.H. Xie, J.K. Shang, J.Q. Jiang, Controlled self-assembly of hollow core-shell FeMn/CoNi Prussian blue analogs with boosted electrocatalytic activity, Small 18 (2022) 2203713.

[16] Y. Shan, G.X. Zhang, W. Yin, H. Pang, Q. Xu, Recent progress in Prussian blue/Prussian blue analogue-derived metallic compounds, B. Chem. Soc. Jpn. 95 (2022) 230–260.

[17] L.L. Ji, J.Y. Wang, X. Teng, T.J. Meyer, Z.F. Chen, CoP nanoframes as bifunctional electrocatalysts for efficient overall water splitting, ACS Catal. 10 (2019) 412–419.

[18] X. Zhang, Y.H. Wu, Y.F. Sun, Q.Y. Liu, L. Tang, J.X. Guo, CoFeP hollow cube as advanced electrocatalyst for water oxidation, Inorg. Chem. Front. 6 (2019) 604–611.

[19] C.J. Xuan, J. Wang, W.W. Xia, Z.K. Peng, Z.X. Wu, W. Lei, K.D. Xia, H.L.L. Xin, D.L. Wang, Porous structured Ni-Fe-P nanocubes derived from a Prussian blue analogue as an electrocatalyst for efficient overall water splitting, ACS Appl. Mater. Interfaces 9 (2017) 26134–26142.

[20] X.Y. Wu, Y. Ru, Y. Bai, G.X. Zhang, Y.X. Shi, H. Pang, PBA composites and their derivatives in energy and environmental applications, Coordin. Chem. Rev. 451 (2022) 214260.

[21] X.Y. Lu, C. Zhao, Electrodeposition of hierarchically structured three-dimensional nickel-iron electrodes for efficient oxygen evolution at high current densities, Nat. Commun. 6 (2015) 1–7.

[22] J.H. Shi, W. Peng, Y.F. Yang, B. Li, J.H. Nie, H. Wan, Y. Li, G.F. Huang, W.Y. Hu, W.Q. Huang, A general strategy for synthesis of binary transition metal phosphides hollow sandwich heterostructures, Small 19 (2023) 2302906.

[23] H. Wang, J.M. Lee, Recent advances in structural engineering of MXene electrocatalysts, J. Mater. Chem. A 8 (2020) 10604–10624.

[24] A.M. Liu, X.Y. Liang, X.F. Ren, W.X. Guan, M.F. Gao, Y.N. Yang, Q.Y. Yang, L.G. Gao, Y.Q. Li, T.L. Ma, Recent progress in MXene-based materials: potential high-performance electrocatalysts, Adv. Funct. Mater. 30 (2020) 2003437.

[25] X.J. Zeng, C. Zhao, Y.C. Yin, T.L. Nie, N.H. Xie, R.H. Yu, G.D. Stucky, Construction of $NiCo_2O_4$ nanosheets-covered $Ti_3C_2T_x$ MXene heterostructure for remarkable electromagnetic microwave absorption, Carbon 193 (2022) 26–34.

[26] X.J. Zeng, X. Jiang, Y. Ning, F.Y. Hu, B.B. Fan, Construction of dual heterogeneous interface between zigzag-like Mo-MXene nanofibers and small CoNi@NC nanoparticles for electromagnetic wave absorption, J. Adv. Ceram. (2023) 10.26599/JAC.2023.9220772.

[27] Y. Tang, C.H. Yang, X.T. Xu, Y.Q. Kang, J. Henzie, W.X. Que, Y. Yamauchi, MXene nanoarchitectonics: Defect-engineered 2D MXenes towards enhanced electrochemical water splitting, Adv. Energy Mater. 12 (2022) 2103867.

[28] B. Zhang, J.W. Shan, X.Y. Wang, Y.J. Hu, Y.Y. Li, Ru/Rh cation doping and oxygen-vacancy engineering of FeOOH nanoarrays@$Ti_3C_2T_x$ MXene heterojunction for highly efficient and stable electrocatalytic oxygen evolution, Small 18 (2022) 2200173.

[29] Y. Tang, C.H. Yang, Y.W. Yang, X.T. Yin, W.X. Que, J.F. Zhu, Three dimensional hierarchical network structure of S-$NiFe_2O_4$ modified few-layer titanium carbides (MXene) flakes on nickel foam as a high efficient electrocatalyst for oxygen evolution, Electrochim. Acta 296 (2019) 762–770.

[30] X.J. Zeng, Y.F. Ye, Y.Q. Wang, R.H. Yu, M. Moskovits, G.D. Stucky, Honeycomb-like MXene/$NiFeP_x$-NC with "continuous" single-crystal enabling high activity and robust durability in electrocatalytic oxygen evolution reactions, J. Adv. Ceram. 12 (2023) 553–564.

[31] N. Li, J.R. Han, K.L. Yao, M. Han, Z.M. Wang, Y.C. Liu, L.H. Liu, H.Y. Liang, Synergistic phosphorized NiFeCo and MXene interaction inspired the formation of high–valence metal sites for efficient oxygen evolution, J. Mater. Sci. Technol. 106 (2022) 90–97.

[32] Q. Yue, J. Sun, S. Chen, Y. Zhou, H.J. Li, Y. Chen, R.Y. Zhang, G.F. Wei, Y.J. Kang, Hierarchical mesoporous MXene-NiCoP electrocatalyst for water splitting, ACS Appl. Mater. Interfaces 12 (2020) 18570–18577.

[33] X.J. Zeng, H.Q. Zhang, R.H. Yu, G.D. Stucky, J.S. Qiu, A phase and interface co-engineered MoP_xS_y@$NiFeP_xS_y$@NPS-C hierarchical heterostructure for sustainable oxygen evolution reaction, J. Mater. Chem. A 11 (2023) 14272–14283.

[34] X.J. Zeng, D.R. Duan, X.F. Zhang, X.H. Li, K. Li, R.H. Yu, M. Moskovits, Doping and interface engineering in a sandwich $Ti_3C_2T_x$/$MoS_{2-x}P_x$ heterostructure for efficient hydrogen evolution, J. Mater. Chem. C 10 (2022) 4140–4147.

[35] J.M. Huang, R.J. Meng, L.H. Zu, Z.J. Wang, N. Feng, Z.Y. Yang, Y. Yu, J.H. Yang, Sandwich-like $Na_{0.23}TiO_2$ nanobelt/Ti_3C_2 MXene composites from a scalable in situ transformation reaction for long-life high-rate lithium/sodium-ion batteries, Nano Energy 46 (2018) 20–28.

[36] X.J. Zeng, C. Zhao, T.L. Nie, Z.Y. Shen, R.H. Yu, G.D. Stucky, Construction of 0D/1D/2D MXene nanoribbons-NiCo@NC hierarchical network and their coupling effect on electromagnetic wave absorption, Mater. Today Phys. 28 (2022) 100888.

[37] P.X. Yan, Y. Hu, E. Shoko, T.T. Isimjan, J.N. Tian, X.L. Yang, Hierarchical core-shell N-doped carbon@FeP_4-CoP arrays as robust bifunctional electrocatalysts for overall water splitting at high current density, Adv. Mater. Interfaces 8 (2021) 2100065.

[38] L. Zhang, X.Y. Wang, A. Li, X.Q. Zheng, L.S. Peng, J.W. Huang, Z.H. Deng, H.M. Chen, Z.D. Wei, Rational construction of macroporous CoFeP triangular plate arrays from bimetal-organic frameworks as high-performance overall water-splitting catalysts, J. Mater. Chem. A 7 (2019) 17529–17535.

[39] Y.Y. Wu, Y. Li, M.K. Yuan, Z. Lü, L.L. Xu, B. Wei, Direct growth of Ni-Fe phosphides nanohybrids on NiFe foam for highly efficient water oxidation, J. Alloy. Compd. 847 (2020) 156363.

[40] F.H. Ma, Q. Wu, M. Liu, L.R. Zheng, F.X. Tong, Z.Y. Wang, P. Wang, Y.Y. Liu, H.F. Cheng, Y. Dai, Z.K. Zheng, Y.C. Fan, B.B. Huang, Surface fluorination engineering of NiFe Prussian blue analogue derivatives for highly efficient oxygen evolution reaction, ACS Appl. Mater. Interfaces 13 (2021) 5142–5152.

[41] X.J. Zeng, Q.Q. Zhang, C.L. Jin, H. Huang, Y.F. Gao, Fe-induced electronic transfer and structural evolution of lotus pod-like $CoNiFeP_x$@P, N-C heterostructure for sustainable oxygen evolution, Energy Environ. Mater. (2023) e12628.

[42] J. Yu, T. Zhang, Y.Q. Sun, X.J. Li, X.Y. Li, B. Wu, D.D. Men, Y. Li, Hollow FeP/Fe_3O_4 hybrid nanoparticles on carbon nanotubes as efficient electrocatalysts for the oxygen evolution reaction, ACS Appl. Mater. Interfaces 12 (2020) 12783–12792.

[43] X.F. Lu, L. Yu, X.W. Lou, Highly crystalline Ni-doped FeP/carbon hollow nanorods as all-pH efficient and durable hydrogen evolving electrocatalysts, Sci. Adv. 5 (2019) eaav6009.

[44] R.Q. Li, B.L. Wang, T. Gao, R. Zhang, C.Y. Xu, X.F. Jiang, J.J. Zeng, Y. Bando, P.F. Hu, Y.L. Li, X.B. Wang, Monolithic electrode integrated of ultrathin NiFeP on 3D strutted graphene for bifunctionally efficient overall water splitting, Nano Energy 58 (2019) 870–876.

[45] M.Y. Dong, H. Qin Fu, Y.M. Xu, Y. Zou, Z.Y. Chen, L. Wang, M.Q. Hu, K.D. Zhang, B. Fu, H.J. Yin, P.R. Liu, H.J. Zhao, NiCo alloy-anchored self-supporting carbon foam as a bifunctional oxygen electrode for rechargeable and flexible Zn-air batteries, Battery Energy 2 (2023) 20220063.

[46] L.B. Xie, L. Hai, Y. Meng, W.W. Zheng, H.P. Hu, D.H. Shang, K. Shao, C.L. Zhang, Y. Li, Metal-atom-doped $W_{18}O_{49}$ nanowires for electrocatalytic oxygen evolution reaction in alkaline medium, ChemPhysMater 2 (2023) 141–147.

[47] S. Zaman, A.I. Douka, L.L. Noureen, X.L. Tian, Z. Ajmal, H.J. Wang, Oxygen reduction performance measurements: discrepancies against benchmarks, Battery Energy 2 (2023) 20220060.

[48] Z.Y. Pan, Z. Tang, Y.Z. Zhan, D. Sun, Three-dimensional porous $CoNiO_2$@reduced graphene oxide nanosheet arrays/nickel foam as a highly efficient bifunctional electrocatalyst for overall water splitting, Tungsten 2 (2020) 390–402.

[49] A.P. Wu, Y. Xie, H. Ma, C.G. Tian, Y. Gu, H.J. Yan, X.M. Zhang, G.Y. Yang, H.G. Fu, Integrating the active OER and HER components as the heterostructures for the efficient overall water splitting, Nano Energy 44 (2018) 353–363.